Flow (2025), **5** E42
doi:10.1017/flo.2025.10033

FLOW CAMBRIDGE
UNIVERSITY PRESS

RESEARCH ARTICLE

Transition mechanisms in hypersonic wind-tunnel nozzles: a methodological approach using global linear stability analysis

Hugo Lemarquand[1], Mathieu Lugrin[1], Cédric Content[2], Clément Caillaud[3], Sébastien Esquieu[3] and Denis Sipp[4]

[1]DAAA ONERA, Institut Polytechnique de Paris, Meudon, France
[2]DAAA ONERA, Institut Polytechnique de Paris, Châtillon, France
[3]CEA-CESTA, 15 Avenue des Sablières, Le Barp, France
[4]ONERA, Institut Polytechnique de Paris, Palaiseau, France
Corresponding author: Hugo Lemarquand; Email: hugo.lemarquand@onera.fr

Received: 18 June 2025; **Revised:** 29 September 2025; **Accepted:** 26 October 2025

Keywords: boundary layer stability; hypersonic Flow; nozzle; resolvent; transition to turbulence; wind-tunnel

Abstract

Base-flow computations and stability analyses are performed for a hypersonic wind tunnel nozzle at a Mach number of 6. Isothermal and adiabatic wall boundary conditions are investigated, and moderate stagnation conditions are used to provide representative scenarios to study the transition in quiet hypersonic wind tunnel facilities. Under these conditions, the studied nozzle shows a small flow separation at the convergent inlet. Global stability analysis reveals that this recirculation bubble may trigger a classical three-dimensional stationary unstable global mode. Resolvent analysis reveals Görtler, first and second Mack modes affecting the divergent part of the nozzle, along with a Kelvin–Helmholtz instability induced by the bubble. The present study also highlights the key impact of perturbations located in the convergent inlet on the development of instabilities further downstream in the divergent outlet, helping to understand the need and efficacy of a suction lip upstream of the nozzle throat to mitigate instabilities in the divergent section. Detailed knowledge of all these mechanisms is essential for understanding flows in quiet hypersonic wind tunnel nozzles and, consequently, represents a key step towards the optimisation of such nozzles.

Impact Statement

Nozzle turbulent boundary layers are a significant source of acoustic noise in conventional hypersonic wind tunnels. They must be avoided when designing ‘quiet’ (low-noise) hypersonic nozzles. The few existing quiet hypersonic wind tunnels are currently limited in Mach number and transition Reynolds number due to this transition, and thus do not fully cover the atmospheric flight conditions required for hypersonic vehicle studies. Consequently, understanding and defining accurate metrics representing the instability potential of a given nozzle design is a crucial point for the optimisation of future higher Reynolds number quiet nozzles. In this article, we provide a spatial high-order tool that computes the base flow of a given nozzle and characterises all possible instabilities, such as globally unstable modes or resolvent modes affecting separated regions and attached boundary layers. For a specific nozzle design, we analyse the various instability mechanisms at play to provide guidelines for the interpretation of such results.

1. Introduction

During the design phase of hypersonic vehicles, wind tunnel testing plays a critical role in validating key factors, such as aerodynamic performance. These tests often focus on investigating the

© The Author(s), 2025. Published by Cambridge University Press. This is an Open Access article, distributed under the terms of the Creative Commons Attribution licence (https://creativecommons.org/licenses/by/4.0/), which permits unrestricted re-use, distribution and reproduction, provided the original article is properly cited.

https://doi.org/10.1017/flo.2025.10033 Published online by Cambridge University Press

laminar-to-turbulent transition of the boundary layer developing on the test model. Accurate prediction of this transition is crucial as the turbulent boundary layer leads to a significant increase in wall heat flux. For example, Van Driest (1956) demonstrated that for a flat plate at Mach 6, the heat flux increases by approximately a factor of five when the boundary layer becomes turbulent. Nowadays, the vast majority of current hypersonic wind tunnels are not sufficiently representative of the atmospheric flight conditions encountered in real-life scenarios, particularly due to limitations in enthalpy levels (Gu and Olivier, 2020). Some facilities allow for the accurate reproduction of similarity parameters such as Mach number, Reynolds number and enthalpy conditions, but fail to replicate the free stream turbulence level. Such fluctuations are known to drastically alter the laminar-to-turbulent transition of the boundary layer on the test model due to the receptivity process (Morkovin, 1969). The receptivity mechanism describes how external disturbances penetrate the boundary layer and establish the initial amplitudes and scales of the instabilities. Consequently, the level of fluctuation in the test section (also referred to as the 'noise level') becomes another new significant similarity parameter. There can be various sources of these disturbances in wind tunnel facilities (Schneider, 2008; Morkovin, 1957), but above Mach 2.5, the primary source of noise is the eddy-Mach-wave radiation from the turbulent boundary layer that develops on the nozzle wall (Laufer, 1961). This noise is approximately 1 to 2 orders of magnitude above flight levels (Schneider, 2008). Chazot *et al.* (2019) illustrate this significant discrepancy in their figure 2, by comparing the noise levels in conventional wind tunnels (VKI H3) to those in quiet wind tunnels (BAM6QT at Purdue University) which achieve noise levels comparable to atmospheric flight conditions (note: flight-level atmospheric fluctuations are $\leq 0.05\,\%$ (Schneider, 2001)). Practically, the effect of noise levels on the boundary layer transition in conventional hypersonic wind tunnels is illustrated by experimental studies of Durant *et al.* (2015) (Figure 12) and McKiernan *et al.* (2021) (Figures 12 and 13). The comparison of TSP (temperature sensitive paint) measurements reveals an early transition on the model in the conventional wind tunnel set-up compared with the low-noise configuration. Thus, one of the main issues in quiet hypersonic wind tunnels is controlling the laminar-to-turbulent transition of the boundary layer on the nozzle wall. Such a control helps to ensure a quiet free stream environment in the test section to closely reproduce atmospheric flight conditions. Currently, such a quiet wind tunnel, in which the laminarity of the boundary layers along the wall is maintained to significantly reduce the noise levels, does exist for Reynolds numbers up to $20 \times 10^6\ \mathrm{m}^{-1}$ at Mach 6 (for example, BAM6QT at Purdue) (Schneider, 2008). However, such facilities are rare, non-existent in Europe (Chazot *et al.*, 2019), and remain limited in both Mach and Reynolds numbers (Schneider, 2008; Beckwith *et al.*, 1986).

As hypersonic wind tunnel nozzles are studied (including the settling chamber, convergent and divergent sections), the boundary layer along the wall evolves from subsonic to supersonic regimes, where various instabilities can develop. Following the classical global linear stability analysis terminology, two families of instabilities can develop in a nozzle: exponential or intrinsic instabilities (oscillatory flow, driven by global modes) and non-normal input–output amplification (noise-amplifier flow, driven by resolvent modes) (Huerre and Monkewitz, 1990). Global modes arise within the flow itself and do not rely on a receptivity mechanism, i.e. no external forcing is introduced in the Navier–Stokes equations. In contrast, resolvent modes depend on a receptivity mechanism and therefore require external disturbances to project sufficient energy on the optimal and sub-optimal forcing structures. A summary of all the potential instabilities that can develop in hypersonic nozzle flows is provided below and summarised in Figure 1. First, Görtler instability can arise over the concave walls of the nozzle (Saric, 1994). Görtler instability is known to be significant and is considered in wind tunnel nozzle design (Schneider, 1998b; Lakebrink *et al.*, 2018; Chen *et al.*, 1985). This instability occurs across all Mach numbers, from incompressible to hypersonic flow conditions, and results from a centrifugal instability mechanism related to the concave curvature of the streamlines (Rayleigh, 1917; Xu *et al.*, 2024). Sipp and Jacquin (2000) have shown that unstable regions that can develop this centrifugal instability are characterised by a negative Rayleigh discriminant ($\Delta < 0$). The Görtler instability is characterised by counter-rotating vortices oriented in the streamwise direction (Görtler, 1941) and these streamwise elongated structures are stationary or at low-frequency (Wu *et al.*, 2011; Xu *et al.*, 2024). This mechanism is sensitive to the disturbance environment (Xu *et al.*, 2024). This instability has been experimentally observed in several wind tunnels at NASA Langley, as reported by Beckwith and Holley (1981) and Beckwith *et al.*

https://doi.org/10.1017/flo.2025.10033 Published online by Cambridge University Press

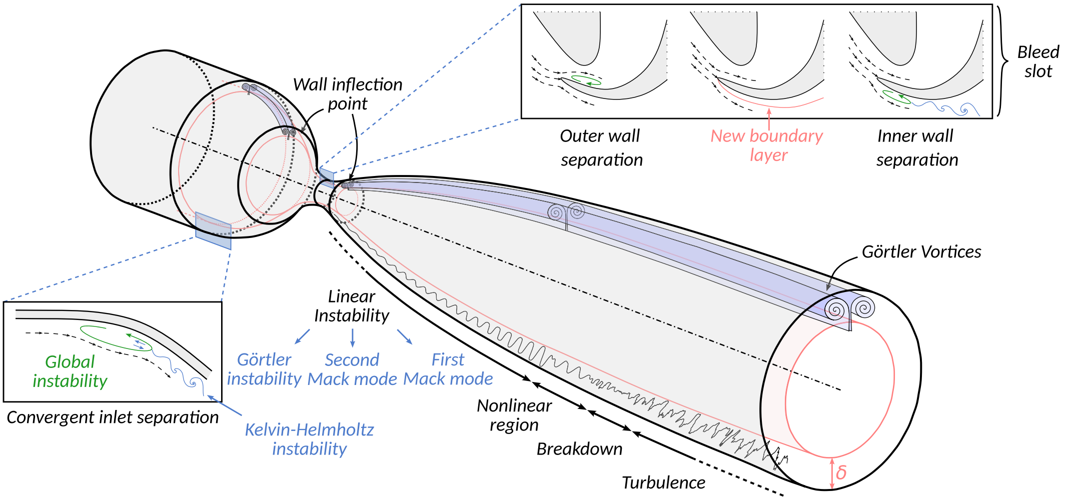

Figure 1. *Schematic of all instabilities within a hypersonic nozzle.*

(1984), showing oil-flow streaks visible on the wall in the convergent section and at the divergent exit (see figures 3, 4 and 9 of Schneider (2008) for precise pictures). A second class of important instabilities is composed of the first and second Mack modes. Stability analyses have shown that such instabilities can grow within hypersonic wind tunnel nozzles (Schneider, 1998b; Schneider *et al.*, 2001; Lakebrink *et al.*, 2018). The oblique (i.e. three-dimensional) first Mack mode corresponds to a viscous inflectional mode, in which fluctuations are localised around the generalised inflection point. In addition to this viscous first mode, Mack (1984) found that multiple inviscid instability modes can exist in the supersonic boundary layer, referred to as the second Mack mode and higher-order modes. The second Mack mode corresponds to a two-dimensional trapped acoustic wave close to the wall and become unstable above $M \approx 4$ (Mack, 1984). Lastly, recirculation bubbles can form at the convergent inlet (Schneider, 1998a) or at the suction lip upstream of the nozzle throat (Taskinoglu *et al.*, 2005; Benay and Chanetz, 2004). These bubbles can lead to new instabilities including global modes (self-sustained in time instabilities that grow exponentially over time) (Marquet *et al.*, 2009; Hildebrand *et al.*, 2018) and convective instabilities such as the Kelvin–Helmholtz instability which arises from the separated shear layer (Barbagallo *et al.*, 2012). Figure 1 offers a summary of all these aforementioned instabilities.

The present work intends to characterise and identify all linear instabilities that can develop in hypersonic wind tunnel nozzles. Therefore, the objective of this study is not to study in detail the laminar-to-turbulent transition process of the boundary layer, i.e. we will not focus on the nonlinear interactions leading to the transition. Instead, we aim to understand how and where linear instabilities develop in the boundary layer, allowing future studies to focus on reducing their growth to delay the transition. Since we are focusing on the early stages of the transition, before nonlinear interactions become dominant, we will therefore use methods based on linear stability theories. Thus, the turbulent boundary layer and all its implications for the flow will not be studied here, note that DNS studies of turbulent boundary layer on hypersonic wind tunnel nozzles have, for example, been carried out by Hildebrand *et al*. (2022) and Duan *et al*. (2019). As for now, most instabilities in hypersonic nozzles, presented in the previous paragraph, are studied using the LST (local stability theory) (Schmid *et al.*, 2002) and the PSE (parabolised stability equations) (Herbert, 1997). However, such methods are only valid for weakly non-parallel flows. Thus, relying on PSE or LST methods to inform an optimisation process, aimed at computing optimal nozzle designs to delay transition, may yield results that do not guarantee the optimality of the computed design due to an incomplete physical representation. Therefore, to address more general configurations, comprehensive methods, such as the resolvent analysis, are available. These methods are increasingly used as they became computationally affordable in the recent years. By construction, the resolvent framework is particularly suited to account for the non-modal growth of instabilities resulting from the non-normality

https://doi.org/10.1017/flo.2025.10033 Published online by Cambridge University Press

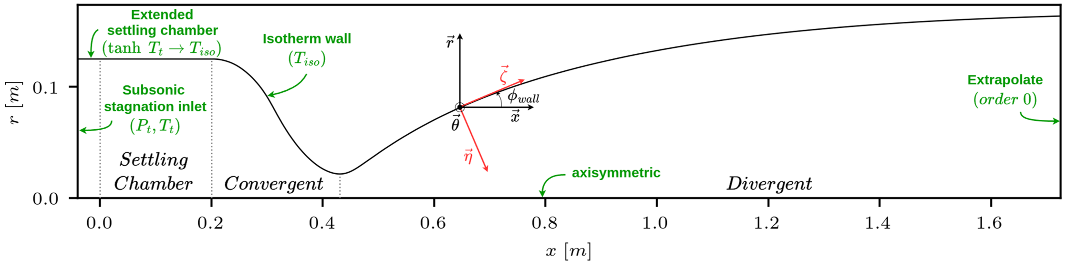

Figure 2. *Numerical set-up for base-flow computation in the isothermal case.*

of the Navier–Stokes operator (Schmid, 2007; Sipp and Marquet, 2013). As this global linear stability framework relies solely on the assumption of linearity, the non-parallel effect is fully accounted for, allowing to accurately probe the effects of flow separation or strong gradients along regions of high wall curvature. Moreover, this global linear stability framework offers a convenient access to the gradients of instabilities amplification with respect to various quantities, a key ingredient for future optimisation work. For instance, this method gives access to the regions of the flow where small modifications to the base flow have the greatest impact on its stability (Marquet *et al.*, 2008; Mettot, 2013; Poulain *et al.*, 2024).

This paper is organised as follows. First, the flow configuration and the nozzle geometry are presented (§ 2). Then, the theoretical aspects and tools used to study both global and resolvent modes using a global linear stability framework (GSA) are introduced (§ 3). In § 4, base flows for the isothermal and adiabatic walls are described. The supplementary material (SM) § SM.3, available at https://doi.org/10.1017/flo.2025.10033, focuses on the study of global modes in the nozzle for both the isothermal and adiabatic cases. In § 5, resolvent modes are studied and identified in the nozzle flow for the isothermal case, followed by a comparison of resolvent modes between the two cases in § SM.4. Finally, in § 6, we will take advantage of the global linear stability tool to demonstrate, through a simple model, the effectiveness of using suction lips upstream of the throat to design quiet wind tunnels.

2. Flow configuration

The nozzle geometry and flow conditions selected to study the linear instabilities that can develop within the boundary layer of hypersonic wind tunnel nozzles are detailed in this section. This nozzle was selected because the flow it produces contains all the instabilities representative of hypersonic wind tunnel flows, e.g. Görtler, and first and second Mack modes. Moreover, it can exhibit, under certain stagnation conditions, a boundary layer separation at the convergent inlet leading to a recirculation bubble. Investigating the effect of such separated regions on instabilities amplification is important for understanding the transition in the nozzle.

The geometry of the hypersonic wind tunnel nozzle used in this study is shown in Figure 2. It is an axisymmetric nozzle from ONERA with a design Mach number of 6. The nozzle consists of three parts: the settling chamber, the convergent and the divergent. Note that the settling chamber length has been increased to accommodate the inlet boundary condition. The dimensions used in this study are therefore not exactly representative of the real configuration. Nevertheless, this part can be seen as a simplified model of a real settling chamber commonly used in this type of wind tunnel (no filter, no supply line, no heater, etc.). Figure 2 also illustrates the two coordinate systems used in this study. The first is the cylindrical coordinate system $(\boldsymbol{e_x}, \boldsymbol{e_r}, \boldsymbol{e_\theta})$ used for base-flow and stability computations. The second is a local coordinate system $(\boldsymbol{e_\zeta}, \boldsymbol{e_\eta}, -\boldsymbol{e_\theta})$ defined with respect to the wall normal and will be used to study the boundary layer and its disturbances.

The inlet boundary condition is set with a stagnation pressure of $P_t = 4$ bar and a stagnation temperature of $T_t = 550$ K. These stagnation conditions represent the lower Reynolds number and temperature range used in this wind tunnel. However, this choice of stagnation conditions provides representative

https://doi.org/10.1017/flo.2025.10033 Published online by Cambridge University Press

scenarios for the study of transition while offering a reduced computational cost. Given the short run time in this type of blowdown-to-vacuum facility and that the nozzle wall is made of steel, the wall temperature is assumed to remain isothermal $T_{iso} = 300$ K. Just before the settling chamber, a zone is added to ensure a smooth variation between the inlet boundary condition at T_t and the wall temperature at T_{iso} using a $\tanh$ function for the wall boundary condition, thus avoiding a temperature bump that is numerically problematic (temperature discontinuity at the upper-left corner). Note that the size of the 'extended settling chamber' shown in Figure 2 has been enlarged for clarity, the length is fixed at 1% of the settling chamber length. The order-0 extrapolation applied at the outlet corresponds to a non-reflecting boundary condition. The base flow is also computed under adiabatic conditions. Although this adiabatic condition may not reflect the physical reality of this flow, it will provide an interesting comparison of wall temperature effects during the stability study.

3. Methods

3.1. Governing equations and linear dynamics

As we are studying axisymmetric wind tunnel nozzles, the cylindrical coordinate system $(\boldsymbol{e_x}, \boldsymbol{e_r}, \boldsymbol{e_\theta})$ is chosen throughout this study. The flow is governed by the compressible Navier–Stokes equations written in conservative form $\partial_t q = R(q)$, with $q = (\rho, \rho u_x, \rho u_r, \rho u_\theta, \rho E)^T$ the state vector of conservative variables (density, momentum and total energy) and $R(q)$ is the discrete residual obtained after spatial discretisation. For more details on this equation, refer to § SM.1.2.1. Note that all variables used are made non-dimensional using length ν_∞ / U_∞, density ρ_∞, velocity U_∞ and temperature T_∞. All are calculated from the reference Mach number M_∞, the stagnation pressure P_t and temperature T_t, and using isentropic flow relations and Sutherland's law (Sutherland, 1893).

To study the linear dynamics of this system, a small three-dimensional (3-D) disturbance $q'(x,r,\theta,t)$ is added to the two-dimensional (2-D) base flow $\overline{q}(x,r)$, which is a steady solution of the governing equation such as $R(\overline{q}) = 0$ and can be seen as a fixed point (equilibrium point). Since the disturbance is assumed to be small compared with the base flow, $q = \overline{q} + \epsilon q'$ with $\epsilon \ll 1$, the nonlinear equation can then be linearised around the base flow $\partial_t q' = \mathcal{J} q'$, where $\mathcal{J}$ is the Jacobian operator around $\overline{q}$ such as $\mathcal{J} = \partial_q R\big|_{\overline{q}}$.

Two families of instabilities can develop in a flow: exponential or intrinsic instabilities (oscillatory flow, driven by global modes) and non-normal input–output amplification (noise-amplifier flow, driven by resolvent modes) (Huerre and Monkewitz, 1990). Even though it is generally known that resolvent modes seem to dominate in wind tunnel nozzle flows, in some cases, it can be interesting to also consider global modes, especially when recirculation bubbles are present (Marquet et al., 2009), as in our case. Two different mathematical approaches are implemented to study these two families of instabilities: the global analysis is presented in § SM.1.1.3, while the resolvent analysis is detailed in the following section.

3.2. Resolvent analysis

The second family of instabilities is termed non-normal input–output amplification (selective noise amplifiers). Even if the flow is globally stable, the flow may exhibit non-modal amplification of convective instabilities at specific frequencies due to the non-normality of the Jacobian operator $\mathcal{J}$ (Schmid, 2007; Sipp and Marquet, 2013). These instabilities depend on the receptivity mechanism and therefore need to be forced to be amplified. A small 3-D forcing perturbation term $f'(x,r,\theta,t)$ (e.g. pressure and/or temperature fluctuations, wall roughness, etc.) is thus added to the Navier–Stokes equation, the new linearised equation is

$$\partial_t q' = \mathcal{J} q' + f'. \tag{1}$$

As the flow is axisymmetric, the θ-direction is supposed to be homogeneous. Hence, these small disturbances can be expressed in Fourier modes of azimuthal wavenumber $m \in \mathbb{Z}$. As the forcing is considered

https://doi.org/10.1017/flo.2025.10033 Published online by Cambridge University Press

harmonic at frequency ω, disturbances can then be expressed as:

$$q'(x,r,\theta,t) = \check{q}(x,r)\, e^{i(m\theta+\omega t)} + c.c. \quad \text{and} \quad f'(x,r,\theta,t) = \check{f}(x,r)\, e^{i(m\theta+\omega t)} + c.c. \tag{2}$$

Equation (1) leads to the following input/output problem $\check{q} = \mathcal{R}(\omega, m)\check{f}$, where $\mathcal{R} = (i\omega I - \mathcal{J})^{-1}$ is the resolvent operator. This operator represents a linear transfer function between the incoming forcing $\check{f}$ (input) and the flow response $\check{q}$ (output). Then, for a given frequency ω and azimuthal wavenumber m, the most amplified resolvent mode is found by solving an optimisation problem defined as a ratio between two energies:

$$\mu^2 = \sup_{\check{f}} \frac{||\check{q}||_E^2}{||\check{f}||_F^2} = \sup_{\check{f}} \frac{||\mathcal{R}\check{f}||_E^2}{||\check{f}||_F^2} = \sup_{\check{f}} \frac{\check{f}^* P^* \mathcal{R}^* Q_E \mathcal{R} P \check{f}}{\check{f}^* Q_F \check{f}}, \tag{3}$$

where μ^2 is the gain, and $||\cdot||_E$ and $||\cdot||_F$ are the norms used to evaluate the energy amplitude of the response and the forcing, respectively. Using a discrete scalar product norm, these norms can be expressed with their Hermitian matrix Q_E and Q_F such as $||\check{q}||_E^2 = \check{q}^* Q_E \check{q}$ and $||\check{f}||_F^2 = \check{f}^* Q_F \check{f}$, where $\check{q}^*$ is the conjugate transpose of $\check{q}$. The Chu energy norm is used for Q_E and Q_F to account for the compressibility effects in the energy measure (Chu, 1965; Hanifi *et al.*, 1996). These matrices are written with conservative variables and are block diagonal (see § SM.1.1 for details). Moreover, to restrict the forcing to a specific area or specific component, we introduce a prolongation matrix P, and define the forcing $\check{f}$ and forcing energy Q_F only on the restricted domain/component. The resulting optimisation problem (3) can be viewed as a Rayleigh quotient and can be recast as a generalised Hermitian eigenvalue problem $P^* \mathcal{R}^* Q_E \mathcal{R} P \check{f}_{opt,i} = \mu_i^2 Q_F \check{f}_{opt,i}$, where μ_i^2, $i \in [[0, \ldots]]$, are the eigenvalues sorted by energy such that $\mu_i^2 \geq \mu_{i+1}^2$. The $\check{f}_{opt,i}$ are the optimal forcing, while $\check{q}_{opt,i} = \mathcal{R} P \check{f}_{opt,i}$ are optimal responses. These two sets of vectors define orthonormal sets of the forcing and response spaces $\check{f}^*_{opt,i} Q_F \check{f}_{opt,j} = \check{q}^*_{opt,i} Q_E \check{q}_{opt,j} = \delta_{ij}$. This eigenvalue problem allows to map the linear system amplification and thus characterise the receptivity of the base flow by solving it for a range of frequencies ω and azimuthal wavenumber m. More details on the global linear stability of dynamical systems are available from Schmid (2007) and Sipp *et al.* (2010). The boundary conditions used for the resolvent analysis are the linearised boundary conditions.

3.3. Numerical methods and strategy

The open-source CFD code BROADCAST (Poulain *et al.*, 2023) is used in this study. This toolbox provides all the tools and numerical methods needed to compute the base-flow and the discrete operators, as well as to perform global linear stability analysis of two-dimensional Cartesian or axisymmetric flows.

After two-dimensional discretisation of the domain into a structured $N_x \times N_r$ mesh, the compressible Navier–Stokes equations are numerically solved using this high-order finite volume solver. This toolbox uses a seventh-order flux-extrapolated MUSCL scheme for the inviscid fluxes (Cinnella and Content, 2016) (validated by Sciacovelli *et al.* (2021) for hypersonic flows), a fourth-order accuracy scheme with a five-point compact stencil for the viscous fluxes (Shen *et al.*, 2009) and algorithmic differentiation (AD) with the software TAPENADE (Hascoet and Pascual, 2013) to extract the discrete direct and adjoint global linear operators (of arbitrary order). The AD tool accurately computes the n-order derivatives of the various operators required for accurate stability analysis (global modes, resolvent modes). A description of the methods used in the BROADCAST toolbox, as well as their validation, can be found from Poulain *et al.* (2023), and has been extended and validated for axisymmetrical flows by Caillaud *et al.* (2025). A reminder of the extension to 3-D stability of the base flow, as well as the definition of the 3-D residual in axisymmetric flows, can be found in § SM.1.2. The base flow is obtained using an iterative pseudo-Newton method as described by Crivellini and Bassi (2011) (see § SM.1.4.2).

https://doi.org/10.1017/flo.2025.10033 Published online by Cambridge University Press

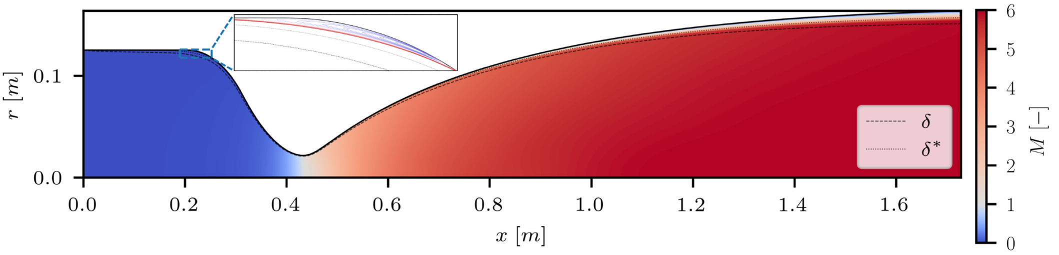

Figure 3. *Base-flow Mach number field for the isothermal case. Zoom-in shows a recirculation bubble at the convergent inlet.*

Details regarding the dimension of the various operators, their memory cost, the methods for solving eigenvalue problems, the nozzle mesh, the numerical simulations and other related information are provided in the supplementary material (see § SM.1.4). This information is not essential for understanding or supporting the manuscript, but may nonetheless be relevant or interesting to readers.

4. Characterisation of the base flow

In this section, the characterisation of the base flow in the hypersonic nozzle for both isothermal and adiabatic cases is performed. A comparison between these two cases is also provided to highlight the differences in the flow induced by these two boundary conditions.

The evolution of the Mach number for the isothermal base flow is shown in Figure 3. A boundary layer separation is observed at the convergent inlet for both isothermal and adiabatic cases, leading to a recirculation bubble in this region. This flow feature is important because recirculation bubbles can trigger global modes and resolvent modes such as Kelvin–Helmholtz instability. For example, the low-frequency instability measured in the NASA Langley Mach-6 quiet nozzle is suspected to come from this kind of separation (Schneider, 1998a; Wilkinson, 1997). Note that the presence of this recirculation bubble here is likely because this wind tunnel was designed to operate at higher stagnation pressures than those used in this study. A comparatively straightforward criterion illustrated in § SM.2.1, known as the Rott–Crabtree method, provides a convenient means to estimate whether boundary layer separation is likely to occur at the convergent inlet. Further details on the base-flow characterisation are provided in § SM.2.

A comparison of the solutions obtained for the two base-flows, under isothermal and adiabatic boundary conditions, is provided in § SM.2.2.

5. Resolvent modes with an isothermal wall

Global analysis (§ SM1.3) of the nozzle flow is performed in § SM.3 to verify the presence or absence of global modes induced by the recirculation bubble in our flow, as it is well known that such flow features can lead to global modes (Theofilis *et al*., 2000; Marquet *et al*., 2009). Global stationary unstable modes, which are highly localised and weakly amplified, have been identified within the recirculation bubble for the isothermal case. These modes are globally unstable for non-zero azimuthal wavenumbers m, implying a three-dimensionalisation of the base flow in the vicinity of the bubble. Consequently, resolvent analysis cannot typically be performed on this flow, as such studies are usually applied to a globally stable flow (i.e. the Jacobian does not exhibit unstable eigenvalues) (Schmid, 2007), which is not our case (in the isothermal case). However, it is important to keep in mind that the goal here is not to characterise the exact transition mechanism of this nozzle (which could be altered due to the globally unstable mode), but rather to identify (using global linear stability analysis) all linear instabilities that can develop in hypersonic wind tunnel nozzles. Therefore, we apply resolvent analysis to examine how such flow would behave if there were no global unstable mode.

https://doi.org/10.1017/flo.2025.10033 Published online by Cambridge University Press

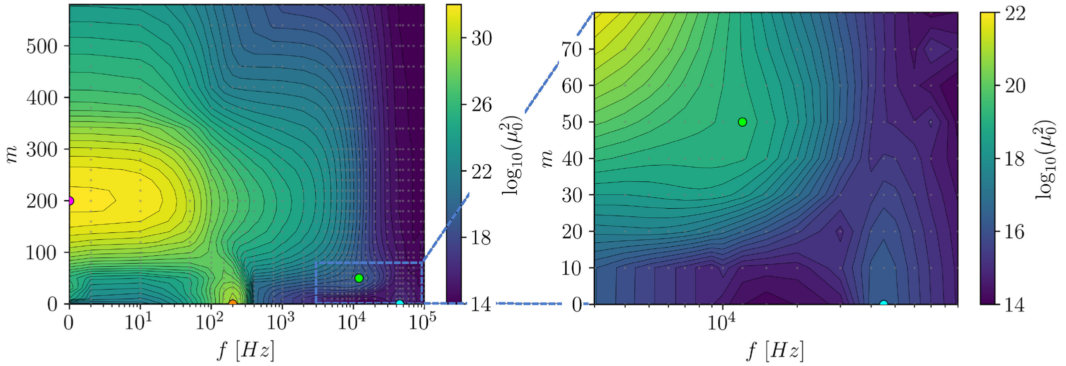

Figure 4. *Optimal gain map μ_0^2 in frequency f and azimuthal wavenumber m space for the isothermal case. The right plot shows the optimal gain map zoom on the area near the first and second Mack modes. The grey dots show the different computation locations. $(f, m) = (0\,Hz, 200)$, Görtler instability peak. $(f, m) = (200\,Hz, 0)$, Kelvin–Helmholtz instability peak. $(f, m) = (12\,kHz, 50)$, first Mack mode peak. $(f, m) = (45\,kHz, 0)$, second Mack mode peak.*

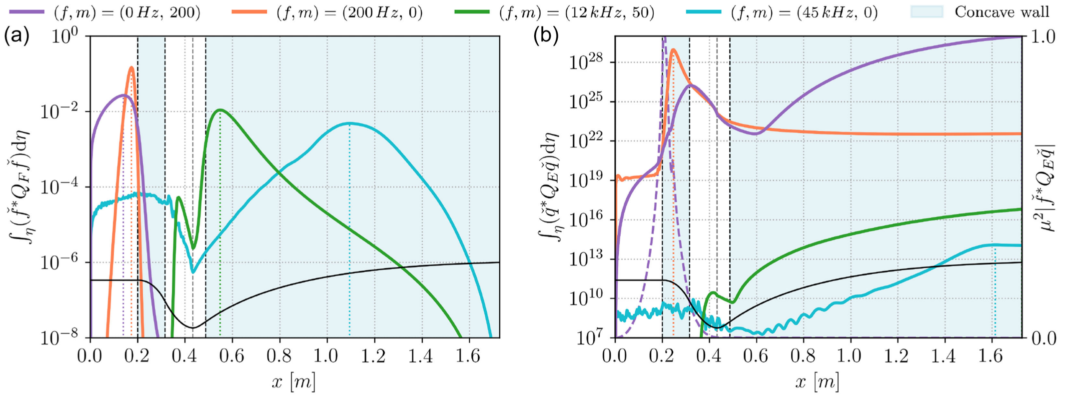

Figure 5. *(Solid lines) Evolution of the quantity E_{Chu} of the (a) optimal forcing and (b) response computed along the gridlines in the r-direction by integrating the local Chu energy contribution. (Dashed line) Evolution of the rate of work done by the forcing onto the response mode $\xi = \mu^2|\check{f}^* Q_E \check{q}|$ computed along the gridlines in the r-direction. $(f, m) = (0\,Hz, 200)$, Görtler instability. $(f, m) = (200\,Hz, 0)$, Kelvin–Helmholtz instability. $(f, m) = (12\,kHz, 50)$, first Mack mode. $(f, m) = (45\,kHz, 0)$, second Mack mode.*

For the numerical set-up, the restriction matrix P is used to exclude the area in front of the settling chamber region ($x < 0$, in Figure 2). Thus, the forcing field can be localised anywhere in the settling chamber and/or convergent and/or divergent of the nozzle. However, the Chu energy matrix Q_E is restricted, in the optimisation problem, to a near-wall region defined by 2δ. This restriction of the Chu energy is applied to only study resolvent modes that develop within the boundary layer and thus not focus on resonant acoustic modes that may exist in the settling chamber and convergent regions due to the confined subsonic flow.

Figure 4 shows the evolution of the optimal gain $\mu_0^2(\omega, m) = \|\check{q}_{opt,0}\|_E^2 / \|\check{f}_{opt,0}\|_F^2$ as a function of frequency f and azimuthal wavenumber m for the isothermal case. Note that the optimal gain μ_0^2 is made non-dimensional by dividing it by the square of the reference time $(\nu_\infty/U_\infty^2)^2$. Four regions of maximum gain can be observed, indicating four dominant mechanisms in our flow, which are the Görtler instability, the Kelvin–Helmholtz instability (shear mode due to the recirculation bubble), and the first and second Mack modes. Figure 5 shows the streamwise evolution of the quantity E_{Chu} (Chu, 1965, see § SM.1.1), computed along the gridlines in the r-direction by integrating the local Chu energy contribution of the

https://doi.org/10.1017/flo.2025.10033 Published online by Cambridge University Press

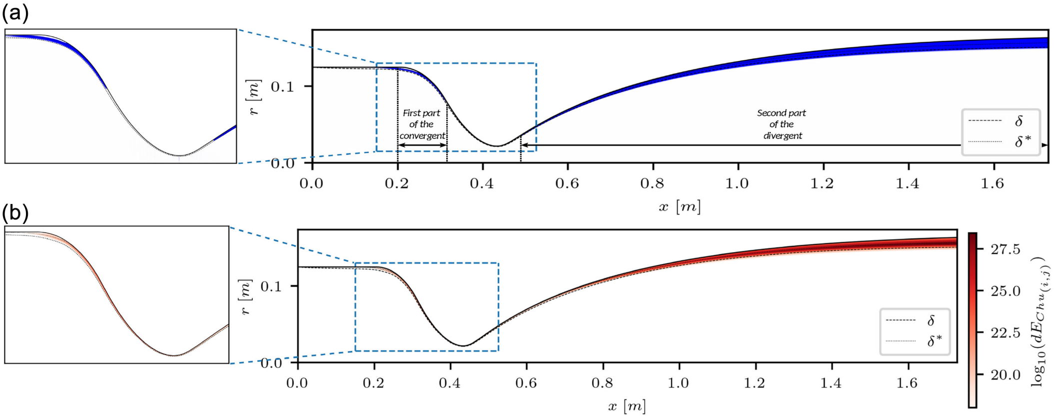

Figure 6. *(a) Blue areas indicate regions in the flow where the Rayleigh discriminant is negative ($\Delta < 0$), i.e. the unstable zones where centrifugal instabilities can develop (Sipp and Jacquin, 2000). Left shows a zoom-in near the throat. (b) Görtler instability $(f, m) = (0\,Hz, 200)$: evolution of the local quantity $E_{Chu_{(i,j)}}$ of the optimal response. Left shows a zoom-in near the throat.*

optimal forcing and response for the four leading mechanisms. In these figures, the blue areas indicate the two concave wall zones: the first part of the convergent and the second part of the divergent. This figure will be referenced in the following sections for discussion of the four dominant mechanisms. In the following sections, we will identify these various resolvent modes in the isothermal case, examining their shapes, locations on the nozzle and other characteristics.

Note that a comparison of the optimal gain maps between the isothermal and adiabatic cases is provided in § SM.4 for readers interested in further details on the resolvent analysis. This section specifically highlights the influence of wall temperature on the development of resolvent modes, as the wall boundary conditions differ between the two cases.

5.1. Görtler instability

The first identified mechanism is the Görtler instability, which peaks at zero frequency (thus stationary) and at an azimuthal wavenumber of $m = 200$. In our case, this is the dominant mechanism, which is not surprising as the nozzle we are studying is known to be relatively short compared with nozzles found in other hypersonic wind tunnels (refer to Figure 27 of Threadgill *et al*. (2024) for a length comparison of this nozzle with a nozzle having the typical length of a quiet wind tunnel nozzle). The short nozzle length implies a significant wall curvature, which promotes the development of centrifugal instability.

To confirm that the observed instability is indeed the Görtler instability, we compute the centrifugal instability criterion known as the Rayleigh discriminant $\Delta = 2\omega_z \|\overline{u}\|/R_{curv}$, with $R_{curv} = \|\overline{u}\|^3/[(\nabla\overline{\psi}) \cdot (\overline{u} \cdot \nabla\overline{u})]$, where $\|\overline{u}\|$ is the norm of the velocity field, $\omega_z = \partial_x u_r - \partial_r u_x$ the vorticity, $\overline{\psi}$ the streamfunction and R_{curv} the local algebraic radius of curvature. Sipp and Jacquin (2000) have demonstrated a sufficient criterion for centrifugal instability using the Rayleigh discriminant: the flow is unstable and can develop centrifugal instabilities where $\Delta < 0$. According to Figure 6a, two regions in the flow can develop centrifugal instabilities, both located near concave wall sections, i.e. the first part of the convergent and the end of the divergent. By looking at the evolution of the local Chu energy $E_{Chu_{(i,j)}}$ of the optimal response at $(f, m) = (0\,\mathrm{Hz}, 200)$, Figure 6b, we can see that the growth in energy occurs in these two $\Delta < 0$ zones. Note that the energy between these two zones corresponds to a decay in energy, as shown in Figure 5, indicating that the instability takes some distance to be advected and dissipates after passing through a suitable centrifugal instability zone. All this confirms that the centrifugal Görtler instability is observed here in the flow. We will now examine in more detail how this instability evolves within the nozzle.

https://doi.org/10.1017/flo.2025.10033 Published online by Cambridge University Press

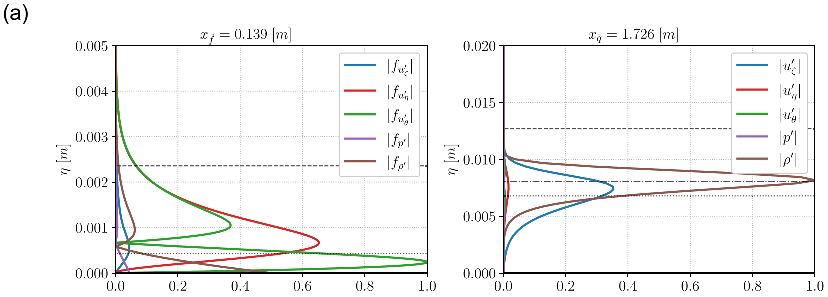

Left: Forcing. Right: Response. (---): boundary layer thickness δ. (······): displacement thickness δ^*. (-·-·-): generalised inflection point.

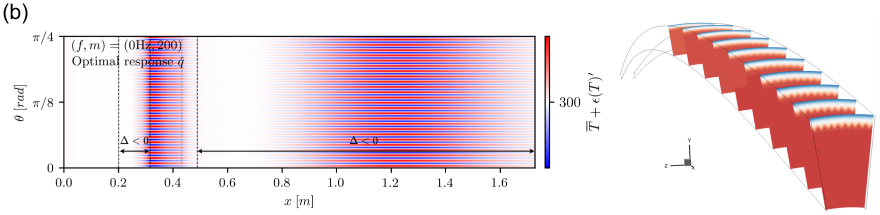

Left: one-eighth of the nozzle wall temperature, i.e. 25 structures since $m = 200$. Right: response $u_\zeta = \overline{u_\zeta} + \epsilon u'_\zeta$ at different x-position in the divergent.

Figure 7. *Görtler instability* $(f, m) = (0\,Hz, 200)$*: (a) eigenfunctions at the maximum Chu energy; (b) plot of* $q = \overline{q} + \epsilon q'$ *with* ϵ *equal to 10 % of the maximum between base flow and fluctuations.*

Figure 5 shows that the forcing peak of the Görtler instability is localised in the settling chamber while the response peak is located at the exit of the divergent section. We can also see that the response grows in the two concave parts of the nozzle. Interestingly, variations in energetic growth are observed in the concave region of the convergent section (two distinct ‘bumps’). However, by computing the localisation of the rate of work done by the forcing onto the response mode, following the Hadamard product formulation as defined by Skene *et al.* (2022), Qadri and Schmid (2017), Houtman *et al.* (2023) and Ribeiro *et al.* (2023), $\xi = \mu^2 |\langle \check{f}, \check{q} \rangle_{Chu}| = \mu^2 |\check{f}^* Q_E \check{q}|$, our analysis reveals that this quantity is predominantly localised on the first ‘bump’. Therefore, the first growth in the concave region of the convergent is attributed to both the base-flow contribution and the rate of work done by the forcing on the response mode, while the second growth in this region is driven solely by the base-flow contribution.

The local eigenfunctions obtained at the maximum Chu energy location are shown in Figure 7a. These eigenfunctions are consistent with the state-of-the-art of Görtler instabilities studied using linear stability (Li *et al.*, 2022; Hao *et al.*, 2023; Cao *et al.*, 2023; Zhao *et al.*, 2024). They are counter-rotating streamwise vortices in the forcing field. While the response mainly exhibits a dominant streamwise structure, slight counter-rotating streamwise vortices still remain in the response. Note that a density peak is also observed for the response along the generalised inflection point. This density peak will also be observed in the study of the first and second Mack modes, which seems to be a property shared by these different instabilities. This property is observed by Hanifi *et al.* (1996) and also noted by Bugeat *et al.* (2019) in a more recent study.

Figure 7b shows the superposition of the base flow and the fluctuations. The evolution of the wall temperature reveals the formation of streaky structures along the wall in the first part of the convergent and the second part of the divergent (i.e. in the regions where the wall is concave, Figure 6a). These structures result from the upwash and downwash effects near the wall induced by the counter-rotating streamwise vortices. This observation aligns with the results reported by Beckwith and Holley (1981) and Beckwith *et al.* (1984) in hypersonic wind tunnels or by Chen *et al.* (2019) on a concave wall. Note that these streaky structures seem to persist for some distance into the convex region of the convergent, as also noted by Schneider (2008). Indeed, the Chu energy associated with the Görtler instability is weakly damped after the concave portion of the convergent, as shown in Figure 5.

https://doi.org/10.1017/flo.2025.10033 Published online by Cambridge University Press

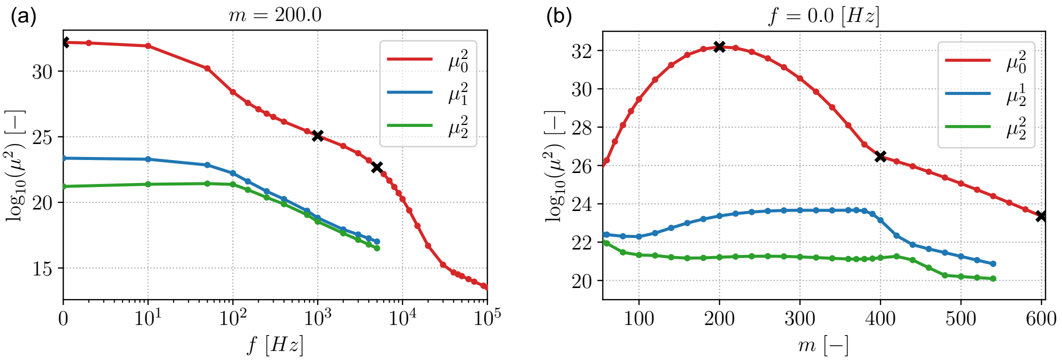

Figure 8. *Optimal μ_0^2 and sub-optimal (μ_1^2 or μ_2^2) gains as a function of: (a) frequency f at a fixed azimuthal wavenumber $m = 200$, (b) azimuthal wavenumber m at a fixed frequency $f = 0$ Hz. The cross markers (×) indicate the points used for the computations in Figures 9a and 9b.*

Consequently, the characteristic structures of the instability are gradually eliminated and advected downstream of the inflection point on the convergent wall section. Figure 7b also reveals that the structures observed at the wall are alternated between the convergent and divergent sections. This variation is likely attributed to the opposite signs of wall curvature in these two regions. Figure 7b, showing the streamwise structures at several slices of the nozzle, clearly reveals the first linear structures commonly identified in Görtler instability studies (Chen *et al.* (2019) study on a concave wall and Li *et al.* (2010) study on a portion of the BAM6QT nozzle). If the nonlinear system is studied, all these structures then evolve through nonlinearities into mushroom-shaped structures usually associated with Görtler vortices.

Before detailing the other resolvent mode mechanisms highlighted in Figures 4 and 5, we provide further insight into the two distinct bumps of the optimal gain μ_0^2, which are clearly noticeable around $(f, m) = (10^3$ Hz, $200)$ and $(f, m) = (10^1$ Hz, $450)$. These peaks suggest the presence of potential physical phenomena occurring in these two specific regions. Given that two regions of the flow can develop centrifugal instabilities, as shown in Figure 6a, the Görtler instability can develop in three possible scenarios: growth of the instability in both $\Delta < 0$ regions (the case discussed above), growth of the instability exclusively in the divergent (second $\Delta < 0$ region) or in the convergent (first $\Delta < 0$ region). The last two possibilities are discussed in the following two paragraphs.

5.1.1. Görtler instability with frequency

The first bump of the optimal gain μ_0^2, near $(f, m) = (10^3$ Hz, $200)$, can be detected in the slice of the optimal gain map Figure 8a. No switch is observed between the optimal gain μ_0^2 and sub-optimal (μ_1^2 or μ_2^2) gains as frequency increases, indicating that there is no change in the leading mechanism between these two bumps but rather a change in mode behaviour. Therefore, the Görtler instability remains the leading mechanism for these frequencies lower than $f = 10$ kHz and $m = 200$.

Examining the streamwise evolution of E_{Chu} of the forcing and response at different frequencies and fixed m, Figure 9a. In contrast, the response appears almost unchanged in terms of energy distribution, with only a Chu energy loss in the divergent and almost no energy contribution from the convergent at higher frequencies. Thus, as the forcing moves downstream in the nozzle, the region where centrifugal instabilities can develop becomes smaller (see Figure 6a), until the instability can only grow in the divergent part of the nozzle (second region where $\Delta < 0$). This leads to a reduction in the Chu energy of the instability and thus a reduction of the optimal gain, leading to the second bump near $f = 10^3$ Hz. Thus, this bump in the optimal gain map μ_0^2 corresponds to the growth of this instability exclusively within the divergent section. This effect will be further validated when studying the restriction of the forcing field in the divergent section (see § 6), where a single gain bump is observed (near $log_{10}(\mu_0^2) = 24.3$) matching the gain bump when the Görtler instability grows exclusively within the divergent at

https://doi.org/10.1017/flo.2025.10033 Published online by Cambridge University Press

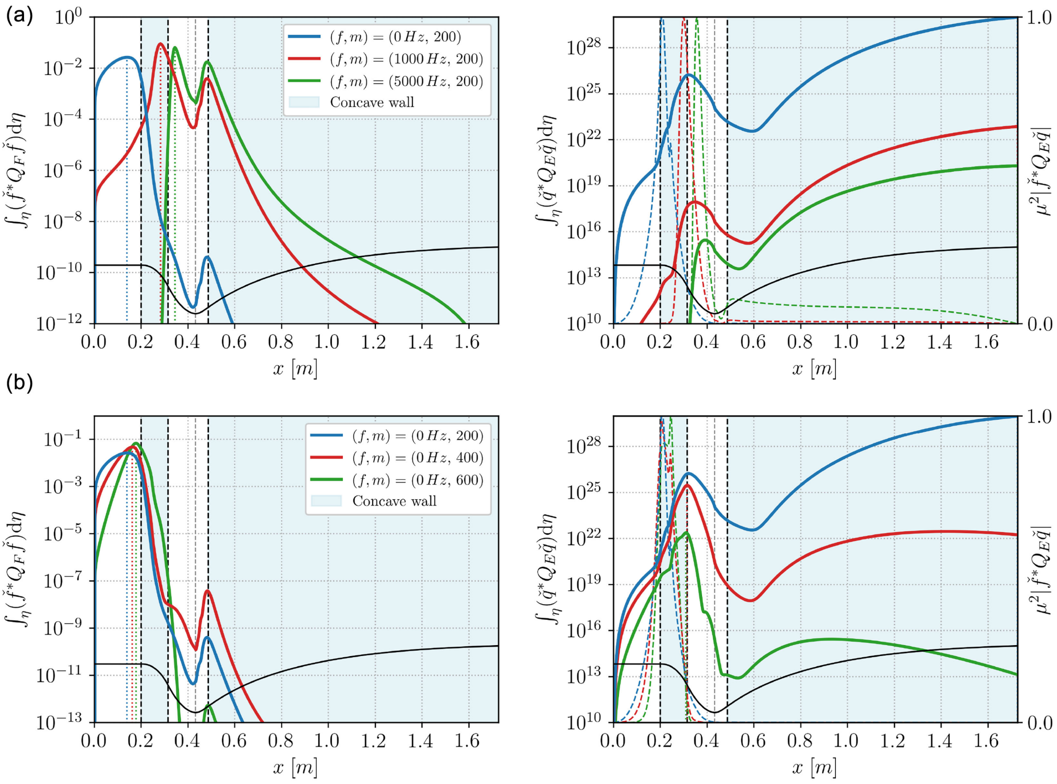

Figure 9. *(Solid lines) Evolution of the quantity E_{Chu} at: (a) different frequencies f and fixed azimuthal wavenumber $m = 200$; (b) different azimuthal wavenumbers m and fixed frequency $f = 0$ Hz of the optimal forcing (left) and response (right) computed along the gridlines in the r-direction by integrating the local Chu energy contribution. (Dashed line) Evolution of the rate of work done by the forcing onto the response mode $\xi = \mu^2 |\check{f}^* Q_E \check{q}|$ computed along the gridlines in the r-direction (normalised by the maximum value for each (f, m)). Frequencies f used in panel (a) and azimuthal wavenumbers m used in panel (b) correspond to the cross markers (×) in Figures 8a and 8b.*

higher frequencies. Note that the increase in Chu energy observed in a non-concave region near the throat for the Görtler instability at $(f, m) = (5000\,\text{Hz}, 200)$ (Figure 9a) originates from the rate of work done by the forcing onto the response mode $\xi = \mu^2 |\check{f}^* Q_E \check{q}|$, rather than from a contribution of the base flow (i.e. suitable curvature).

5.1.2. Görtler instability with azimuthal wavenumber

Next, the second gain bump on the optimal gain map in Figure 4, located around $(f, m) = (10^1\ \text{Hz},\ 450)$, is examined. To better visualise this bump, a slice of the optimal gain map at zero frequency is shown in Figure 8b. As in the previous case, no change between the optimal and sub-optimal gains is observed, suggesting that there is no change in mode but rather a change in behaviour. This supports that the Görtler instability is still observed here.

By applying the same approach as in the previous case, but this time examining the streamwise evolution of E_{Chu} as a function of the azimuthal number m at a fixed frequency $f = 0$ Hz, as shown in Figure 9b, it is observed that as m increases, the forcing remains essentially unchanged and localised in the settling chamber, while the response shifts upstream within the nozzle until the maximum of Chu's energy is no longer located in the divergent but rather in the convergent. Specifically focusing on the divergent region, it is also noticeable that the peak disturbance energy moves also upstream, towards

https://doi.org/10.1017/flo.2025.10033 Published online by Cambridge University Press

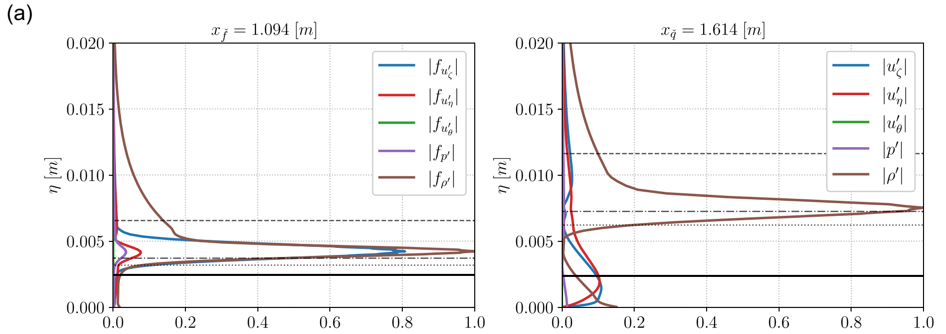

Left: Forcing. Right: Response. (---): boundary layer thickness δ. (⋯⋯): displacement thickness δ^*. (-·-·): generalised inflection point. (—): $\hat{M} = -1$, the supersonic region is located below this line.

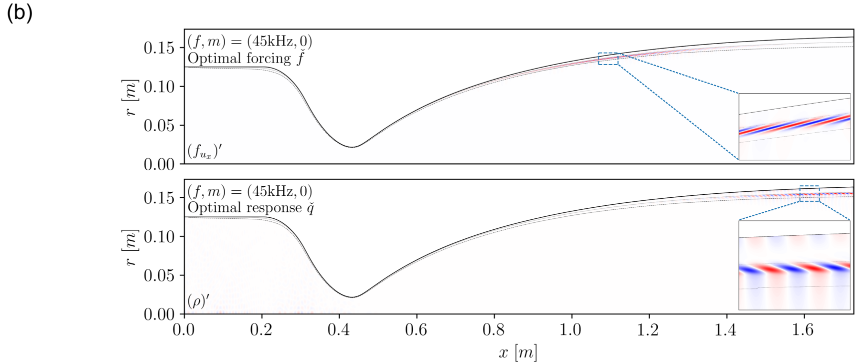

Top: streamwise $f_{u'_x}$ optimal forcing. Bottom: density ρ' optimal response. Zoom: on the area near maximum Chu energy for the forcing and the response. (---): boundary layer thickness δ. (⋯⋯): displacement thickness δ^*.

Figure 10. *Second Mack mode* $(f, m) = (45\ kHz, 0)$*: (a) eigenfunctions at the maximum Chu energy; (b) eigenfunctions field in the nozzle.*

the region where the boundary layer is thinner. The following conclusion is drawn: this increase of the azimuthal number m leads the Görtler instability to adapt to the thinner boundary layers localised in the convergent and the beginning of the divergent (Figure SM2), due to the link between the azimuthal wavenumber m and the boundary layer thickness δ. As a result, the instability can almost exclusively grow in the first $\Delta < 0$ zone located in the first part of the convergent, with limited growth in the second $\Delta < 0$ region as it can no longer adapt to the thicker boundary layer at the end of the divergent section. This adaptation explains the gain reduction observed around $m = 400$ and the second bump in the optimal gain map.

5.2. Second Mack mode instability

Having identified and understood the dominant instability in our flow, attention can now turn to the other resolvent modes, specifically the high-frequency peak observed on the optimal gain map in Figure 4. This instability, peaking at $m = 0$ (i.e. axisymmetric) and around $f = 45$ kHz, corresponds to the second Mack mode. The estimated frequency, determined using the resolvent analysis, aligns with the estimation provided by Mack (1984), where $f = U_e/2\delta$. The second Mack mode is the least amplified instability compared with others examined in this study, which is consistent with findings from previous Mach-6 wind tunnel investigations (Schneider, 1998b; Lakebrink *et al.*, 2018; Schneider *et al.*, 2001). Indeed, this mode is known to develop above $M \approx 4$ (Mack, 1984), a condition reached only in a limited portion of the divergent section due to the short length of the studied nozzle.

The eigenfunctions obtained at the maximum of the Chu energy for the second Mack mode (Figure 5) are presented in Figure 10a. The maximum forcing and response are located in the divergent section. The shape of these eigenfunctions and their interpretation are consistent with the results by

https://doi.org/10.1017/flo.2025.10033 Published online by Cambridge University Press

Bugeat *et al.* (2019) on a flat plate. To compute the relative Mach number $\hat{M}$, the method proposed by Bugeat *et al*. (2019) is employed. Thus, a supersonic region of relative Mach number $\hat{M} < -1$ is detected close to the wall for both forcing and response fields, which is a condition for the existence of additional unstable modes according to Mack (1984). The optimal response fluctuations $\check{q}$ grow within this near-wall supersonic region, while the density is also amplified near the generalised inflection point. This property of the density is also observed in other instabilities and in other studies (Hanifi *et al*., 1996; Bugeat *et al*., 2019). Moreover, the optimal forcing disturbances $\check{f}$ are not localised in this supersonic region but are instead concentrated along the generalised inflection point. Bugeat *et al*. (2019) concluded that it seems that there are two distinct mechanisms coexisting. The first mechanism is specific to the second Mack mode and corresponds to the growth of hydrodynamic and thermodynamic disturbances in the supersonic region. The second is an inflectional mechanism, where thermodynamic disturbances are also amplified along the generalised inflection point.

The axisymmetric fluctuation structures of the second Mack mode, illustrated in Figure 10b, align with the linear stability results from the resolvent analyses on a flat plate (Poulain *et al*., 2023; Bugeat *et al*., 2019), as well as with the results comparing LST and DNS obtained by Egorov *et al.* (2006, 2007) and Unnikrishnan and Gaitonde (2020), showing the classic two-lobed structure of second-mode instability. Moreover, Figure 5 reveals acoustic disturbance structures within the subsonic region of the nozzle (oscillating/noisy curve in the subsonic region). This phenomenon, observed only for the second Mack mode, results in a slight contribution of Chu energy (Figure 5) for both the forcing and the response. This energy contribution is relatively small compared with the energy in the divergent section. Consequently, this study has not identified any significant synchronisation between acoustic mode resonances in the subsonic region and the second Mack mode.

5.3. First mack mode instability

Another gain peak is observed around $(f, m) = (12\,\text{kHz}, 40)$. Given that both the frequency and the azimuthal wavenumber are non-zero, this corresponds to an oblique mode. This instability matches the characteristics of the first Mack mode. The maximum forcing and response are located in the divergent section, Figure 5. The eigenfunctions for this first Mack mode, extracted at the peak Chu energy, are shown in Figure 11a. These eigenfunctions are consistent with the findings from the flat plate study using the resolvent analysis by Bugeat *et al.* (2019). The forcing exhibits a dominant transverse component, whereas the response is mainly longitudinal with a streamwise velocity response. The optimal response is localised near the generalised inflection point of the boundary layer, which is characteristic of the first Mack mode (Mack, 1984). Figure 11b highlights a reorientation of the disturbance structures between the forcing and the response fields, interpreted as the action of the non-modal Orr mechanism. The numerical estimation of the oblique angle of the perturbation is $\Psi \approx 73^\circ$, which is consistent with commonly observed waves angles for this instability (Mack, 1984).

5.4. Kelvin–Helmholtz instability

The last mechanism identified in this nozzle is a low-frequency instability at $f = 200\,\text{Hz}$, which peaks at zero azimuthal wavenumber for the isothermal case. This instability is attributed to the Kelvin–Helmholtz instability arising from the recirculation bubble at the convergent inlet. Figure 5 shows that the maximum optimal forcing occurs in the settling chamber just before the boundary layer separation, while the response is located in the convergent section immediately downstream of the recirculation bubble. Examination of the disturbance structures associated with this mode, see Figure 12, reveals that the instability emanates from the recirculation bubble displaying the characteristic structures of the Kelvin–Helmholtz instability. The results obtained regarding the linear structures of the Kelvin–Helmholtz instability, which emerge from a recirculation bubble, are consistent with studies using resolvent analysis in backward-facing step flows (Dergham *et al*., 2013; Barbagallo *et al*., 2012) and laminar separation bubbles around aerofoils (Thomareis and Papadakis, 2018).

https://doi.org/10.1017/flo.2025.10033 Published online by Cambridge University Press

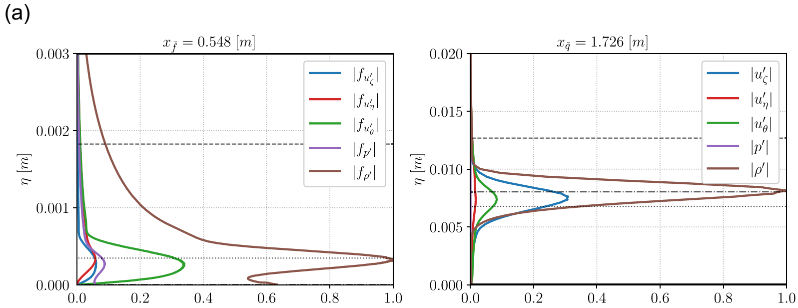

Left: Forcing. Right: Response. (---): boundary layer thickness δ. (⋯⋯): displacement thickness δ^*. (-·-·-): generalised inflection point.

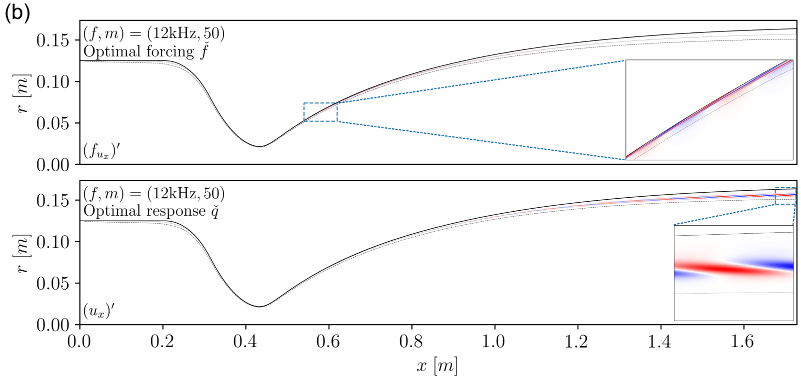

Top: streamwise $f_{u'_x}$ optimal forcing. Bottom: streamwise u'_x optimal response. Zoom on the area near maximum Chu energy for the forcing and the response. (---): boundary layer thickness δ. (⋯⋯): displacement thickness δ^*.

Figure 11. *First Mack mode* $(f, m) = (12\ kHz, 50)$*: (a) eigenfunctions at the maximum Chu energy; (b) eigenfunctions field in the nozzle.*

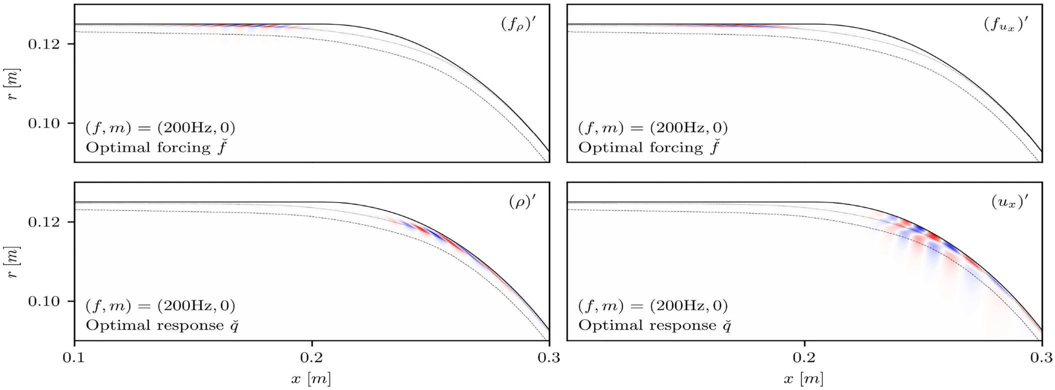

Figure 12. *Kelvin–Helmholtz instability, shear mode due to the recirculation bubble,* $(f, m) = (200\ Hz, 0)$*, eigenfunctions field near the convergent inlet. Top: density* $f_{\rho'}$ *and streamwise* $f_{u'_x}$ *optimal forcing. Bottom: density* ρ' *and streamwise* u'_x *optimal response. (Dashed lines) Boundary layer thickness* δ*. (Dotted lines) Displacement thickness* δ^**.*

This low-frequency instability observed here may explain the low-frequency instability that persisted in the Mach-6 NASA Langley nozzle (Wilkinson, 1997), because, as noticed by Schneider *et al.* (2001), the separation bubble that could appear in wind tunnel contractions are usually unstable and thus would transmit noise downstream.

https://doi.org/10.1017/flo.2025.10033 Published online by Cambridge University Press

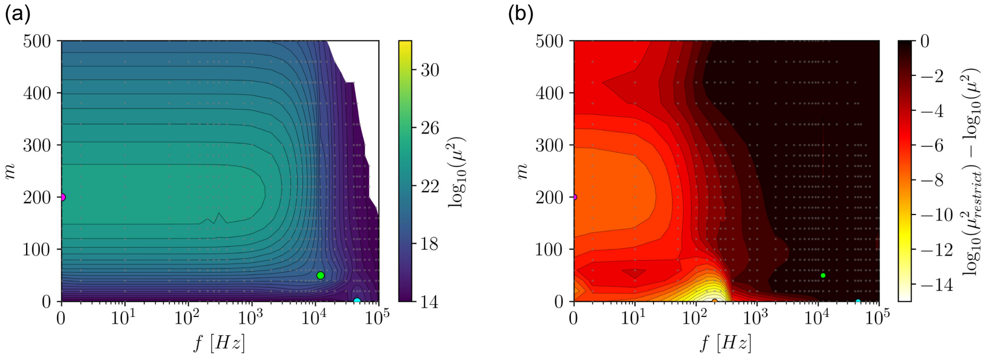

Isothermal case restricted to the divergent section.

Difference in the optimal gain with and without restrictions.

Figure 13. *(a) Optimal gain map μ_0^2 in frequency f and azimuthal wavenumber m space with the forcing field restricted to the divergent section. (b) Difference between the optimal gain map with the forcing field restricted to the divergent section and the optimal gain map in Figure 4 without restriction of the forcing field, in the isothermal case. The grey dots show the different computation locations. $(f, m) = (0\,Hz, 200)$, Görtler instability peak. $(f, m) = (200\,Hz, 0)$, Kelvin–Helmholtz instability peak. $(f, m) = (12\,kHz, 50)$, first Mack mode peak. $(f, m) = (45\,kHz, 0)$, second Mack mode peak.*

6. Forcing field restricted to the divergent section only

This section models the influence of a boundary layer suction slot, a device used in all quiet hypersonic wind tunnel nozzles to bleed off the instability or the turbulent boundary layer that may develop in the settling chamber and/or convergent parts of the nozzle. It is an extremely effective device that has enabled the achievement of quiet wind tunnels (Schneider, 2008; Beckwith, 1975; Chen *et al*., 1993). If the boundary layer suction slot upstream of the throat is closed, the flow returns to a noisy state (Chen *et al*., 1993) (see also Figure 3 of Liu and Yi (2024) for a clear experimental visualisation, which highlights the crucial role of this suction slot on the boundary layer transition).

To model this, the restriction matrix P is applied, limiting the forcing field to the divergent section (from throat to outlet). Therefore, all disturbances originating from the settling chamber and/or the convergent parts are eliminated, which is precisely the goal of the suction slot upstream of the throat. Although the suction slot would in reality create a new boundary layer, which is not modelled here, this simplification remains realistic due to the thinness of the boundary layer in the throat region. Moreover, this simple model also eliminates the necessity of including the suction lip in the simulation with all the complexities it involves (Taskinoglu *et al*., 2005; Benay and Chanetz, 2004): boundary layer separation, meshing, etc. It is therefore a relatively simple model to implement, allowing us to draw conclusions.

The restricted gain map, Figure 13a, shows significant differences compared with the unrestricted case in Figure 4. With the restriction, the Görtler instability shows a single bump in the optimal gain map, indicating growth only in the divergent section as the instability can now develop only within a single negative Rayleigh discriminant zone ($\Delta < 0$) located in the divergent section (see Figure 6a). This outcome aligns with the results of resolvent analyses by Hao *et al.* (2023) and Cao *et al*. (2023), where only one $\Delta < 0$ zone is present. This behaviour had already been observed earlier during the study of Görtler instability variations with frequency (see § 5.1.1). Figure SM8a shows that this single bump corresponds to the second bump in the unrestricted case at higher frequencies (near $log_{10}(\mu_0^2) = 24.3$), thereby supporting earlier observations. Figure SM8b confirms the expected decrease in optimal gain with increasing azimuthal wavenumber m, as the instability adapts to thinner upstream boundary layer.

Figure 13b, which compares optimal gains with and without the restriction, illustrates the impact of the convergent section on the development of resolvent modes. The Görtler instability exhibits non-negligible growth in the convergent section. The Kelvin–Helmholtz instability, associated with the recirculation bubble, has completely disappeared in the restricted case, as expected since the restriction

https://doi.org/10.1017/flo.2025.10033 Published online by Cambridge University Press

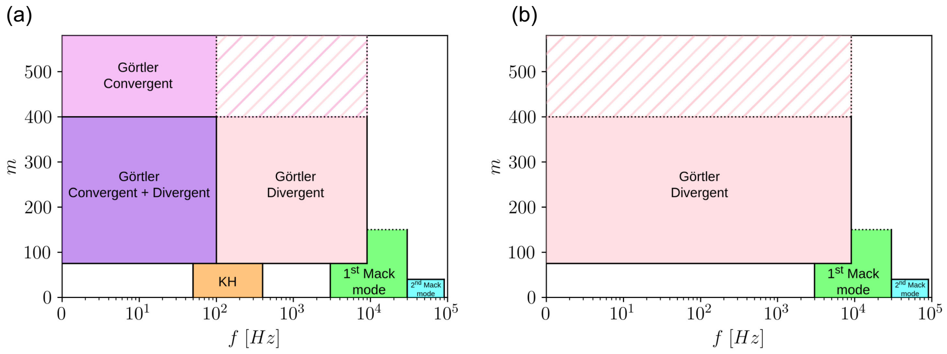

Isothermal case.

Isothermal case restricted to the divergent.

Figure 14. *Simplified overview of Figures 4 and 13, showing the optimal gain μ_0^2 in frequency f and azimuthal wavenumber m space.*

eliminates all disturbances originating from the settling chamber or convergent section. However, the first and second Mack modes remain unaffected, as their forcing and response fields are located mainly in the divergent section (see Figure 5).

This simplified model highlights the essential role of a boundary layer suction slot upstream of the nozzle throat. The clear difference in optimal gain between restricted and unrestricted cases shows that, when properly implemented, the suction slot effectively eliminate all instabilities originating from the settling chamber or convergent section. By doing so, it delays the development of boundary layer instabilities and thus postpones the onset of turbulence boundary layer along the nozzle wall.

7. Conclusion and future work

In this paper, all linear instabilities that may develop within the boundary layer of hypersonic wind tunnel nozzles (see Figure 1), including both global modes (recirculation bubble mode) and resolvent modes (Görtler, Kelvin–Helmholtz, and first and second Mack modes) are characterised and identified using global linear stability analysis. A summary of all identified resolvent modes and their corresponding locations on the optimal gain map, for both restricted and unrestricted cases, is provided in Figure 14.

First, the eigenvalue analysis of the Jacobian operator has highlighted global modes that may develop within recirculation bubbles. These recirculation bubbles can form at the convergent inlet and on the inner or outer walls of the bleed slot upstream of the throat. Such separations may compromise the proper operation of the wind tunnel by introducing new instabilities that could lead to an early transition of the boundary layer.

Second, resolvent analysis was performed on the base flow, enabling the identification and characterisation of resolvent modes. The Görtler instability was identified as the dominant instability. It can develop in two distinct zones suitable for the development of centrifugal instability, located where there is a concave wall i.e. in the first part of the convergent section and the second part of the divergent section. The peak of the Görtler instability is characterised by a streamwise mode at zero frequency (i.e. stationary) and a non-zero azimuthal number (i.e. three-dimensional). For this instability, it was observed that as the frequency increases, the optimal forcing shifts downstream in the nozzle until the instability only develops in the divergent section. However, as the azimuthal wavenumber increases, the instability scales to thinner boundary layers and can no longer develop in the thicker boundary layer at the end of the divergent section. The first and second Mack modes were also identified in the nozzle. Both of these instabilities develop in the divergent section and their characteristics are consistent with previous state-of-the-art results. The last identified instability is the Kelvin–Helmholtz instability, which arises from the recirculation bubble. This instability can be controlled in such flows by ensuring the suppression of recirculation bubbles.

https://doi.org/10.1017/flo.2025.10033 Published online by Cambridge University Press

Finally, the restriction of the forcing field to the divergent section provided a simple model for the implementation of a bleed slot upstream of the nozzle throat. This device enables the suppression of the instability or the turbulent boundary layer that may develop in the settling chamber and/or convergent parts of the nozzle by creating a new boundary layer at the lip. It was found that the Görtler instability grows only in the concave part of the divergent section and is strongly damped compared with the case without restriction, as the instability cannot develop in the convergent section of the nozzle. This study illustrates the impact of the convergent section on the development of resolvent modes. As a result, the optimal gain for the Görtler instability is significantly reduced and the Kelvin–Helmholtz instability is completely eliminated. However, the first and second Mack modes remain unaffected by this device, as their energy is located almost exclusively in the divergent section of the nozzle.

The prospect of this work is to take advantage of the global linear stability framework to conduct optimisation studies for these nozzles. For example, discrete sensitivity analysis of the optimal resolvent gain based on the Hessian of the Navier–Stokes equation around the base flow provides insights into the regions of the flow where small modifications to the base flow have the greatest impact on its stability (Mettot, 2013; Marquet *et al.*, 2008; Poulain *et al.*, 2024). Using the Hessian operator, optimisation strategies (such as volume control, wall temperature, wall blowing/suction, etc.) could then be considered to optimally reduce instability growth. Additionally, sensitivity studies focused on nozzle geometry could also be performed using the formalism proposed by Kitzinger *et al.* (2023) to find an optimal wall contour to delay the transition. It would also be interesting for future work to develop an inlet boundary conditions resolvent-based approach (i.e. a case where the forcing is likely not optimal). This framework would differ from the volumetric forcing approach used here and move closer to a configuration more representative of wind tunnel experiments, for example, by introducing a decomposition of the inlet disturbances into entropic, vortical or measurement-related components, etc. Such an approach would provide a more realistic description of the problem.

Supplementary material. The supplementary material for this article can be found at https://doi.org/10.1017/flo.2025.10033.

Acknowledgements. We are grateful to Arthur Poulain for his development of the open-source CFD code BROADCAST.

Funding statement. This study was supported by funding from ONERA and CEA-CESTA.

Competing interests. The authors declare no conflict of interest.

Data availability statement. Data that support the findings of this study are available by the authors upon reasonable request.

References

Barbagallo, A., Dergham, G., Sipp, D., Schmid, P. J., & Robinet, J.-C. (2012). Closed-loop control of unsteadiness over a rounded backward-facing step. *Journal of Fluid Mechanics*, *703*, 326–362.

Beckwith, I. E. (1975). Development of a high reynolds number quiet tunnel for transition research. *AIAA Journal*, *13*(3), 300–306.

Beckwith, I. E., Chen, F.-J., Creel, J. R., & T. (1986). Design requirements for the nasa langley supersonic low-disturbance wind tunnel. In *14th aerodynamic testing conference* (p. 763).

Beckwith, I. E., & Holley, B. B. (1981). *Görtler vortices and transition in wall boundary layers of two mach 5 nozzles*. NASA STI/Recon TR 1869, Vol. 81, Paper 3150.

Beckwith, I. E., Malik, M. R., & Chen, F.-J. (1984). Nozzle optimization study for quiet supersonic wind tunnels. In *17th fluid dynamics, plasma dynamics, and lasers conference* (p. 1628).

Benay, R., & Chanetz, B. (2004). Design of a boundary layer suction device for a supersonic quiet wind tunnel by numerical simulation. *Aerospace Science and Technology*, *8*(4), 255–271.

Bugeat, B., Chassaing, J.-C., Robinet, J.-C., & Sagaut, P. (2019). 3d global optimal forcing and response of the supersonic boundary layer. *Journal of Computational Physics*, *398*, 108888.

Caillaud, Cément, Scholten, A., Kuehl, J., Paredes, P., Lugrin, M., Esquieu, Sébastien, Li, F., Choudhari, M. M., Benitez, E. K., Borg, M. P., McDaniel, Z. A., Jewell, J. S. (2025). Separation and transition on a cone-cylinder-flare: Computational investigations. *AIAA Journal*, *63*(7), 2615–2634.

Cao, S., Hao, J., Guo, P., Wen, C.-Y., & Klioutchnikov, I. (2023). Stability of hypersonic flow over a curved compression ramp. *Journal of Fluid Mechanics*, *957*, A8.

https://doi.org/10.1017/flo.2025.10033 Published online by Cambridge University Press

Chazot, O., Gülhan, A., Hannemann, K., McGillvray, M., Serre, L., Tran, P., & Steelant, J. (2019). Need for low-noise high-speed facilities in europe. In *1st international conference on flight vehicles, aerothermodynamics and re-entry missions and engineering (FAR)*.

Chen, F.-J., Malik, M. R., & Beckwith, I. E. (1985). Instabilities and transition in the wall boundary layers of low-disturbance supersonic nozzles. In *18th fluid dynamics and plasmadynamics and lasers conference* (p. 1573).

Chen, F.-J., Wilkinson, S. P., & Beckwith, I. E. (1993). Görtler instability and hypersonic quiet nozzle design. *Journal of Spacecraft and Rockets*, *30*(2), 170–175.

Chen, X., Huang, G., & Lee, C. (2019). Hypersonic boundary layer transition on a concave wall: Stationary görtler vortices. *Journal of Fluid Mechanics*, *865*, 1–40.

Chu, B.-T. (1965). On the energy transfer to small disturbances in fluid flow (part i). *Acta Mechanica*, *1*(3), 215–234.

Cinnella, P., & Content, C. (2016). High-order implicit residual smoothing time scheme for direct and large eddy simulations of compressible flows. *Journal of Computational Physics*, *326*, 1–29.

Crivellini, A., & Bassi, F. (2011). An implicit matrix-free discontinuous galerkin solver for viscous and turbulent aerodynamic simulations. *Computers & Fluids*, *50*(1), 81–93.

Dergham, G., Sipp, D., & Robinet, J.-C. (2013). Stochastic dynamics and model reduction of amplifier flows: The backward facing step flow. *Journal of Fluid Mechanics*, *719*, 406–430.

Duan, L., Choudhari, M. M., Chou, A., Munoz, F., Radespiel, R., Schilden, T., Schröder, W., Marineau, E. C., Casper, K. M., Chaudhry, R. S., Candler, G. V., Gray, K. A., Schneider, S. P. (2019). Characterization of freestream disturbances in conventional hypersonic wind tunnels. *Journal of Spacecraft and Rockets*, *56*(2), 357–368.

Durant, A., André, T., Schneider, S. P., & Chynoweth, B. C. (2015). Mach 6 quiet tunnel laminar to turbulent investigation of a generic hypersonic forebody. In *20th AIAA international space planes and hypersonic systems and technologies conference* (p. 3575).

Egorov, I., Fedorov, A., Novikov, A., & Soudakov, V. (2007). Direct numerical simulation of supersonic boundary-layer stabilization by porous coatings. In *45th AIAA aerospace sciences meeting and exhibit* (p. 948).

Egorov, I., Fedorov, A., & Soudakov, V. (2006). Direct numerical simulation of disturbances generated by periodic suction-blowing in a hypersonic boundary layer. *Theoretical and Computational Fluid Dynamics*, *20*, 41–54.

Görtler, H. (1941). Instabilität laminarer grenzschichten an konkaven wänden gegenüber gewissen dreidimensionalen störungen. *ZAMM-Journal of Applied Mathematics and Mechanics/Zeitschrift für Angewandte Mathematik Und Mechanik*, *21*(4), 250–252.

Gu, S., & Olivier, H. (2020). Capabilities and limitations of existing hypersonic facilities. *Progress in Aerospace Sciences*, *113*, 100607.

Hanifi, A., Schmid, P. J., & Henningson, D. S. (1996). Transient growth in compressible boundary layer flow. *Physics of Fluids*, *8*(3), 826–837.

Hao, J., Cao, S., Guo, P., & Wen, C.-Y. (2023). Response of hypersonic compression corner flow to upstream disturbances. *Journal of Fluid Mechanics*, *964*, A25.

Hascoet, L., & Pascual, V. (2013). The tapenade automatic differentiation tool: Principles, model, and specification. *ACM Transactions On Mathematical Software (TOMS)*, *39*(3), 1–43.

Herbert, T. (1997). Parabolized stability equations. *Annual Review of Fluid Mechanics*, *29*(1), 245–283.

Hildebrand, N., Choudhari, M. M., Deegan, C. P., Huang, J., & Duan, L. (2022). Direct numerical simulation of acoustic disturbances in a hypersonic two-dimensional nozzle configuration. *AIAA Journal*, *60*(6), 3452–3463.

Hildebrand, N., Dwivedi, A., Nichols, J. W., Jovanović, M. R., & Candler, G. V. (2018). Simulation and stability analysis of oblique shock-wave/boundary-layer interactions at mach 5.92. *Physical Review Fluids*, *3*(1), 013906.

Houtman, J., Timme, S., & Sharma, A. (2023). Resolvent analysis of a finite wing in transonic flow. *Flow*, *3*, E14.

Huerre, P., & Monkewitz, P. A. (1990). Local and global instabilities in spatially developing flows. *Annual Review of Fluid Mechanics*, *22*(1), 473–537.

Kitzinger, E., Sipp, D., Marquet, O., & Piot, E. (2023). Receptivity of swept-aerofoil flows to small-amplitude wall roughness using a transfer function from wall displacements to induced velocity perturbations. *Flow*, *3*, E41.

Lakebrink, M. T., Bowcutt, K. G., Winfree, T., Huffman, C. C., & Juliano, T. J. (2018). Optimization of a mach-6 quiet wind-tunnel nozzle. *Journal of Spacecraft and Rockets*, *55*(2), 315–321.

Laufer, J. (1961). Aerodynamic noise in supersonic wind tunnels. *Journal of the Aerospace Sciences*, *28*(9), 685–692.

Li, F., Choudhari, M. M., Chang, C.-L., Greene, P., & Wu, M. (2010). Development and breakdown of gortler vortices in high speed boundary layers. In *48th AIAA aerospace sciences meeting including the new horizons forum and aerospace exposition* (p. 705).

Li, F., Choudhari, M. M., & Paredes, P. (2022). Secondary instability of görtler vortices in hypersonic boundary layer over an axisymmetric configuration. *Theoretical and Computational Fluid Dynamics*, *36*(2), 205–235.

Liu, X., & Yi, S. (2024). Experimental investigation about the aerodynamic noise caused by hypersonic turbulence. *Physics of Fluids*, *36*(1), 016101.

Mack, L. M. (1984). Boundary-layer linear stability theory. *Agard Reports*, *709*(3), 1–3.

Marquet, O., Lombardi, M., Chomaz, J.-M., Sipp, D., & Jacquin, L. (2009). Direct and adjoint global modes of a recirculation bubble: Lift-up and convective non-normalities. *Journal of Fluid Mechanics*, *622*, 1–21.

https://doi.org/10.1017/flo.2025.10033 Published online by Cambridge University Press

Marquet, O., Sipp, D., & Jacquin, L. (2008). Sensitivity analysis and passive control of cylinder flow. *Journal of Fluid Mechanics*, *615*, 221–252.

McKiernan, G. R., Chynoweth, B. C., Schneider, S. P., Berridge, D. C., & Wheaton, B. M. (2021). Boundary layer transition preflight experiments in a mach-6 quiet tunnel. *Journal of Spacecraft and Rockets*, *58*(1), 54–66.

Mettot, C. (2013). Linear stability, sensitivity, and passive control of turbulent flows using finite differences (*PhD thesis*, Ecole polytechnique. Thèse de doctorat dirigée par Sipp, Denis Mécanique des fluides Palaiseau, Ecole polytechnique 2013).

Morkovin, M. V. (1957). On transition experiments at moderate supersonic speeds. *Journal of the Aeronautical Sciences*, *24*(7), 480–486.

Morkovin, M. V. 1969, On the many faces of transition. In *Viscous drag reduction: proceedings of the symposium on viscous drag reduction held at the LTV Research Center, Dallas, Texas, September 24 and 25, 1968,* (pp. 1–31). Springer.

Poulain, A., Content, Cédric, Sipp, D., Rigas, G., Garnier, E. (2023). Broadcast: A high-order compressible cfd toolbox for stability and sensitivity using algorithmic differentiation. *Computer Physics Communications*, *283*, 108557.

Poulain, A., Content, Cédric, Rigas, G., Garnier, E., Sipp, D. (2024). Adjoint-based linear sensitivity of a supersonic boundary layer to steady wall blowing–suction / heating–cooling. *Journal of Fluid Mechanics*, *978*, A16.

Qadri, U. A., & Schmid, P. J. (2017). Frequency selection mechanisms in the flow of a laminar boundary layer over a shallow cavity. *Physical Review Fluids*, *2*(1), 013902.

Rayleigh, L. (1917). On the dynamics of revolving fluids. *Proceedings of the Royal Society of London. Series A, Containing Papers of a Mathematical and Physical Character*, *93*(648), 148–154.

Ribeiro, J. M., Yeh, C.-A., & Taira, K. (2023). Triglobal resolvent analysis of swept-wing wakes. *Journal of Fluid Mechanics*, *954*, A42.

Saric, W. S. (1994). Görtler vortices. *Annual Review of Fluid Mechanics*, *26*(1), 379–409.

Schmid, P. J. (2007). Nonmodal stability theory. *Annual Review of Fluid Mechanics*, *39*, 129–162.

Schmid, P. J., Henningson, D. S., & Jankowski, D. (2002). Stability and transition in shear flows. *Applied Mathematical Sciences*, *55*(3), B57–B59.

Schneider, S. P. (1998a). Design and fabrication of a 9.5-inch mach-6 quiet-flow ludwieg tube. In *20th AIAA advanced measurement and ground testing technology conference* (p. 2511).

Schneider, S. P. (1998b). Design of a mach-6 quiet-flow wind-tunnel nozzle using the e**n method for transition estimation. In *36th AIAA aerospace sciences meeting and exhibit* (p. 547).

Schneider, S. P. (2001). Effects of high-speed tunnel noise on laminar-turbulent transition. *Journal of Spacecraft and Rockets*, *38*(3), 323–333.

Schneider, S. P. (2008). Development of hypersonic quiet tunnels. *Journal of Spacecraft and Rockets*, *45*(4), 641–664.

Schneider, S. P., Rufer, S., Randall, L., & Skoch, C. (2001).Shakedown of the purdue mach-6 quiet-flow ludwieg tube. In *39th aerospace sciences meeting and exhibit* (p. 457).

Sciacovelli, L., Passiatore, D., Cinnella, P., & Pascazio, G. (2021). Assessment of a high-order shock-capturing central-difference scheme for hypersonic turbulent flow simulations. *Computers & Fluids*, *230*, 105134.

Shen, Y., Zha, G., & Chen, X. (2009). High order conservative differencing for viscous terms and the application to vortex-induced vibration flows. *Journal of Computational Physics*, *228*(22), 8283–8300.

Sipp, D., & Jacquin, L. (2000). Three-dimensional centrifugal-type instabilities of two-dimensional flows in rotating systems. *Physics of Fluids*, *12*(7), 1740–1748.

Sipp, D., & Marquet, O. (2013). Characterization of noise amplifiers with global singular modes: The case of the leading-edge flat-plate boundary layer. *Theoretical and Computational Fluid Dynamics*, *27*, 617–635.

Sipp, D., Marquet, O., Meliga, P., & Barbagallo, A. (2010). Dynamics and control of global instabilities in open-flows: A linearized approach. *Applied Mechanics Reviews*, *63*(3), 030801.

Skene, C. S., Yeh, C.-A., Schmid, P. J., & Taira, K. (2022). Sparsifying the resolvent forcing mode via gradient-based optimisation. *Journal of Fluid Mechanics*, *944*, A52.

Sutherland, W. (1893). Lii. the viscosity of gases and molecular force. *The London, Edinburgh, and Dublin Philosophical Magazine and Journal of Science*, *36*(223), 507–531.

Taskinoglu, E., Knight, D., & Schneider, S. P. (2005). Numerical analysis of the bleed slot design of the purdue mach 6 wind tunnel. In *43rd AIAA aerospace sciences meeting and exhibit* (p. 901).

Theofilis, V., Hein, S., & Dallmann, U. (2000). On the origins of unsteadiness and three-dimensionality in a laminar separation bubble. *Philosophical Transactions of the Royal Society of London. Series A: Mathematical, Physical and Engineering Sciences*, *358*(1777), 3229–3246.

Thomareis, N., & Papadakis, G. (2018). Resolvent analysis of separated and attached flows around an airfoil at transitional reynolds number. *Physical Review Fluids*, *3*(7), 073901.

Threadgill, J. A., Hader, C., Singh, A., Tsakagiannis, V., Fasel, H. F., Little, J. C., Lugrin, M., Bur, R., Chiapparino, G., & Stemmer, C. (2024). Scaling and transition effects on hollow-cylinder/flare sblis in wind tunnel environments. In *AIAA SCITECH 2024 forum* (pp. 0498).

Unnikrishnan, S., & Gaitonde, D. V. (2020). Linear, nonlinear and transitional regimes of second-mode instability. *Journal of Fluid Mechanics*, *905*, A25.

Van Driest, E. R. (1956). *The problem of aerodynamic heating*. Institute of the Aeronautical Sciences Los Angeles.

https://doi.org/10.1017/flo.2025.10033 Published online by Cambridge University Press

Wilkinson, S. P. (1997). A review of hypersonic boundary layer stability experiments in a quiet mach 6 wind tunnel. In *28th fluid dynamics conference* (p. 1819).

Wu, X., Zhao, D., & Luo, J. (2011). Excitation of steady and unsteady görtler vortices by free-stream vortical disturbances. *Journal of Fluid Mechanics*, *682*, 66–100.

Xu, D., Ricco, P., & Duan, L. (2024). Görtler instability and transition in compressible flows. *AIAA Journal*, *62*(2), 489–517.

Zhao, G., Ma, T., Chen, Z., Zhang, Z., Hao, J., & Wen, C.-Y. (2024). Investigation of streamwise streak characteristics over a compression ramp at mach 4. *Physics of Fluids*, *36*(10), 104121.

Cite this article: Lemarquand H., Lugrin M., Content C., Caillaud C., Esquieu S. and Sipp D. (2025). Transition mechanisms in hypersonic wind-tunnel nozzles: a methodological approach using global linear stability analysis. *Flow*, *5*, E42. https://doi.org/10.1017/flo.2025.10033

https://doi.org/10.1017/flo.2025.10033 Published online by Cambridge University Press